Nano Research
2023, 16(11): 12745–12752

ISSN 1998-0124 CN 11-5974/O4
https://doi.org/10.1007/s12274-023-6144-6

Research Article

Hollow multishelled structural TiN as multi-functional catalytic host for high-performance lithium-sulfur batteries

Wei Xu[1,2], Ruyi Bi[1,2], Mei Yang[1,4], Jiangyan Wang[1,3,4] (✉), Ranbo Yu[2] (✉), and Dan Wang[1,3,4] (✉)

[1] *State Key Laboratory of Biochemical Engineering, Institute of Process Engineering, Chinese Academy of Sciences, Beijing 100190, China*
[2] *School of Metallurgical and Ecological Engineering, University of Science and Technology Beijing, Beijing 100083, China*
[3] *School of Chemical Engineering, University of Chinese Academy of Sciences, Beijing 100049, China*
[4] *Key Laboratory of Biopharmaceutical Preparation and Delivery, Chinese Academy of Sciences, Beijing 100190, China*

Received: 6 July 2023 / **Revised:** 30 August 2023 / **Accepted:** 30 August 2023

ABSTRACT

Lithium-sulfur (Li-S) battery has attracted extensive attention because of its ultrahigh theoretical energy density and low cost. However, its commercialization is seriously hampered by its short cycling life, mainly due to the shuttle of soluble lithium polysulfides (LiPSs) and poor rate capability due to sluggish reaction kinetics. Although significant efforts have been devoted to solving the problems, it is still challenging to simultaneously address all the issues. Herein, titanium nitride hollow multishelled structure (TiN HoMS) sphere is designed as a multi-functional catalytic host for sulfur cathode. TiN, with good conductivity, can effectively catalyze the redox conversion of S and LiPSs, while its surficial oxidation passivation layer can strongly anchor LiPSs. Besides, HoMS enables TiN nanoparticle subunits to expose abundant active sites for anchoring and promoting conversion of LiPSs, while the multiple shells provide physical barriers to restrict the shuttle effect. In addition, HoMS can buffer the volume expansion of sulfur and shorten the charge transport pathway. As a result, the sulfur cathode based on triple-shelled TiN HoMS exhibits an initial specific capacity of 1016 mAh·g^{-1} at a high sulfur loading of 2.8 mg·cm^{-2} and maintains 823 mAh·g^{-1} after 100 cycles. Moreover, it shows a four times higher specific capacity than the one without TiN host at 2 C.

KEYWORDS

lithium-sulfur batteries, titanium nitride, hollow multishelled structure, shuttle effect, rate capability

1 Introduction

Lithium-sulfur (Li-S) battery, which possesses a high theoretical energy density of 2600 Wh·kg^{-1}, abundant sulfur storage, low cost, and environmentally friendliness, has drawn intensive interest [1–5]. However, Li-S battery suffers from a series of challenges, such as poor rate capability due to the low electrical conductivity of S and sluggish reaction kinetics. More severely, the large volume expansion of S and the shuttle of long-chain lithium polysulfide (LiPS) intermediates cause short cycling lifespan and low S utilization, which seriously hinders the commercialization of Li-S batteries [6–13]. Great efforts have been devoted to solving these problems, mainly including design of novel S cathode architecture, binder optimization, electrolyte component optimization, or the use of solid-state electrolyte [14, 15]. Typically, hollow structured materials have been extensively employed as S host in Li-S batteries [16–24]. The large internal cavity buffers the volume expansion of S during lithiation process, while the polar metal compounds are capable of adsorbing polysulfides. Wherein, hollow multishelled structures (HoMS) with multiple ordered shells have been proven promising for as S host as well as multiple other application fields [25–30]. For example, Wang's group developed a TiO_{2-x} as S host [25], which provides more adsorption and redox active sites and restricts the shuttle of LiPSs effectively. Additionally, porous thin shells can shorten the electron and ion transport paths [31–41]. Nonetheless, most metal compound hollow materials possess poor electrical conductivity and limited active centers. Therefore, the performance of Li-S battery still remains to be improved.

Herein, we develop TiN HoMS for the first time as multi-functional catalytic host for S cathode. As shown in Scheme 1, such polar TiN HoMS host has abundant desirable advantages: (1) TiN has an excellent electrical conductivity of up to 55,000 S·cm^{-1}, and it enables catalytic conversion of LiPSs after their adsorption and capture, further promoting redox reactions [42–47]; (2) TiN can anchor LiPSs via forming N–S bonds, in addition, its naturally formed surficial oxide passivation layer could also anchor LiPSs via forming S–Ti–O bonds, thus effectively inhibiting the shuttle of LiPSs [48, 49]; (3) the large internal cavity of HoMS significantly buffers the volume expansion of S material during lithiation [50, 51]; and (4) the HoMS could increase the contact area between TiN and active substances, providing more adsorption and redox active sites [52, 53]. As a result, the Li-S battery, by adopting triple-shelled TiN HoMS as S host, exhibits an initial specific capacity of 1016 mAh·g^{-1} under a high sulfur loading of 2.8 mg·cm^{-2} and the specific capacity maintains at 823 mAh·g^{-1} after 100 cycles. More impressively, a much better rate capability than the one without S host is achieved.

2 Results and discussion

TiN HoMSs were fabricated through a sequential templating

Address correspondence to Jiangyan Wang, jywang@ipe.ac.cn; Ranbo Yu, ranboyu@ustb.edu.cn; Dan Wang, danwang@ipe.ac.cn

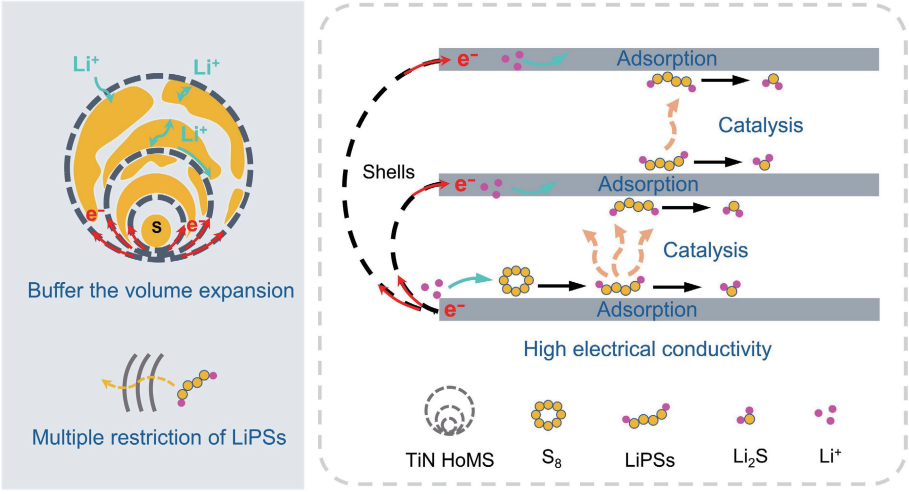

Scheme 1 Schematic illustration of the electrode process for the S@3s-TiN HoMS cathode.

approach (STA), which has been proven quite fruitful for HoMS synthesis [54–57], followed by a nitride treatment. Firstly, TiO_2 HoMSs were synthesized by the STA method, as reported in Refs. [30, 58, 59], which were then nitrided to become TiN using melamine as nitrogen source. Figures 1(a)–1(c) show transmission electron microscopy (TEM) images of TiO_2 hollow sphere (HS) and double- and triple-shelled (2s- and 3s-) TiO_2 HoMS, respectively. The multishelled structure was well-maintained after being nitrided (Figs. 1(e)–1(g)) to obtain TiN HoMS. As characterized by scanning electron microscopy (SEM) (Figs. 1(d)

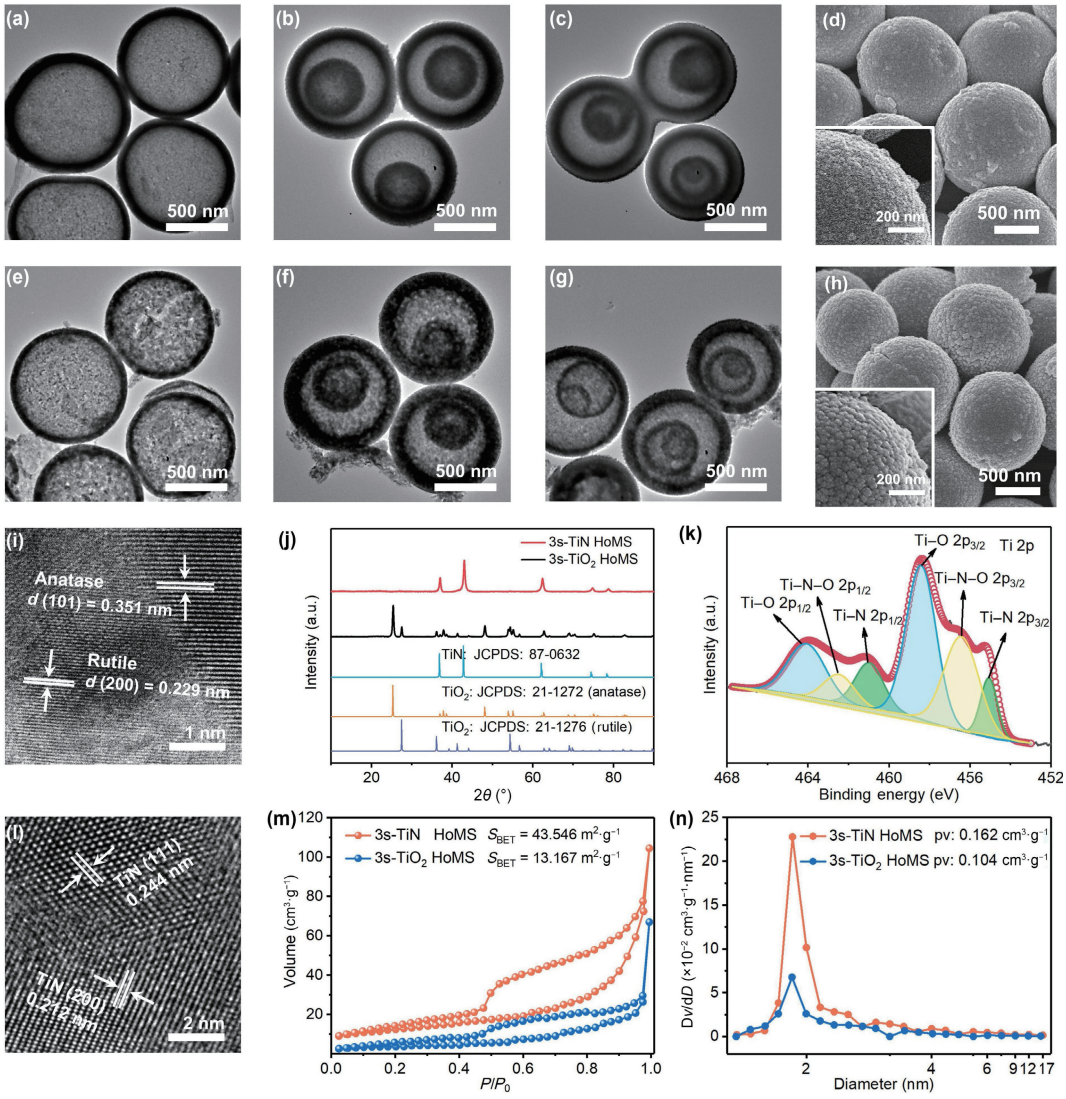

Figure 1 TEM images of (a) TiO_2 HS, (b) 2s-, and (c) 3s-TiO_2 HoMS. (d) SEM images of 3s-TiO_2 HoMS. TEM images of (e) TiN HS, (f) 2s-, and (g) 3s-TiN HoMS. (h) SEM images of 3s-TiN HoMS. The HRTEM images of (i) 3s-TiO_2 HoMS and (l) 3s-TiN HoMS. (j) Powder XRD patterns of 3s-TiO_2 HoMS and 3s-TiN HoMS. (k) Ti 2p XPS spectra of 3s-TiN HoMS. (m) Nitrogen adsorption–desorption isotherms and (n) Barret–Joyner–Halenda (BJH) pore-size distribution curves of the as-prepared 3s-TiO_2 HoMS and 3s-TiN HoMS.

and 1(h)), both shells of TiO_2 HoMS and TiN HoMS are composed of nanosized grains. X-ray diffraction (XRD) patterns (Fig. 1(j)) and the high-resolution TEM (HRTEM) (Fig. 1(i)) indicate that 3s-TiO_2 HoMS is composed of anatase and rutile phase, while only the peaks of TiN without any impurity phases are detected in the TiN HoMS sample, which indicates the total transformation of TiO_2 HoMS to TiN HoMS after nitridation treatment. In addition, clear lattice fringes with an inter-planar spacing of 0.212 and 0.244 nm are observed in the HRTEM (Fig. 1(l)), which is assigned to the (200) and (111) planes, respectively, of TiN [42]. X-ray photoelectron spectroscopy (XPS) test was also performed on TiN HoMS (Fig. 1(k) and Fig. S4 in the Electronic Supplementary Material (ESM)). The signals at 460.98 and 455.08 eV are ascribed to the Ti–N configuration, and the peaks at 462.48 and 456.44 eV are attributed to the Ti–N–O species. In addition, there are two signals at 464.08 and 458.42 eV, corresponding to the Ti–O signals of TiO_2, which may be due to that oxide layer is formed on the surface of TiN when it is exposed to ambient air [42]. What is more interestingly, Brunauer–Emmett–Teller (BET) N_2 adsorption–desorption analysis (Fig. 1(m), and Fig. S3 and Table S1 in the ESM) shows that the specific surface area of TiN HoMS is three times that of TiO_2 HoMS. In addition, the pore size distribution indicates that TiN HoMS possesses more mesopores (Fig. 1(n)). The higher specific surface area and more mesopores of TiN HoMS are favorable for anchoring sulfur and LiPSs.

The S@TiN composite was synthesized by a melting-diffusion method, and details could be found in the ESM. TiN HoMS maintains its original spherical shape after S loading, and the contrast within the cavity between shells is obviously darkened compared to bare TiN samples (Figs. 2(a)–2(c)). Energy-dispersive X-ray (EDX) element mapping (Fig. 2(d)) proves that S has been successfully loaded into the internal space of TiN hollow sphere. The linear scan analysis of S@2s-TiN HoMS composite further proves the presence of high content of S distributed in the cavity of TiN HoMS (Figs. 2(e) and 2(f)). In addition, sharp XRD peaks of S were detected in the S@TiN composite, suggesting that crystalline S has been successfully encapsulated into TiN HoMS (Fig. 2(g)). Thermogravimetric analysis shows that the loading mass ratios of S in the S@TiN HS, S@2s-TiN HoMS, and S@3s-TiN HoMS are about 65.4%, 70.3%, and 80.1%, respectively. The higher S loading of the 3s-TiN HoMS may be that its multiple shells could better inhibit the S loss comparable to TiN HS during the washing process to remove the surface residual S.

To compare the LiPS adsorption ability of different samples, parallel adsorption measurements were performed by placing the same mass amount of samples into Li_2S_6 solution (5 mmol·L^{-1}). After 12 h of immersion, the color of the solution added with TiN-nanoparticle (NP) turned lighter (Fig. 3(a)) but remained yellowish. Comparatively, solutions containing TiN HS or HoMS turned colorless, which may be because that TiN HS or HoMS possesses a larger specific surface area and better adsorption of Li_2S_6. The ultraviolet–visible (UV–Vis) spectral characterization (Fig. 3(a)) further confirmed the above results. The chemical interaction mechanism between titanium nitride and LiPSs was

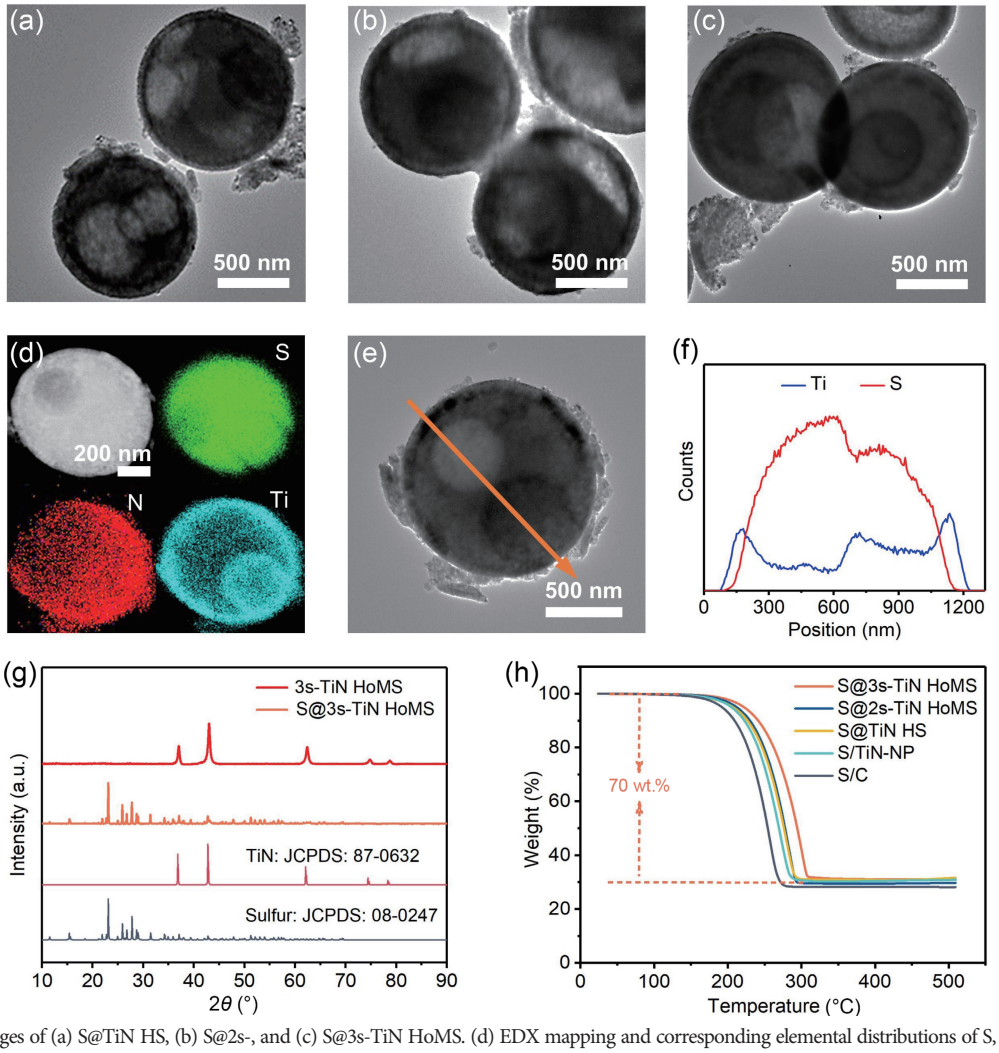

Figure 2 TEM images of (a) S@TiN HS, (b) S@2s-, and (c) S@3s-TiN HoMS. (d) EDX mapping and corresponding elemental distributions of S, N, and Ti of S@2s-TiN HoMS. (e) TEM image of S@2s-TiN HoMS and (f) linear distributions of S and Ti along the arrow line on (e). (g) Powder X-ray diffraction patterns of 3s-TiN HoMS and S@3s-TiN HoMS. (h) Thermogravimetric analysis of S@TiN HS and S@TiN HoMS.

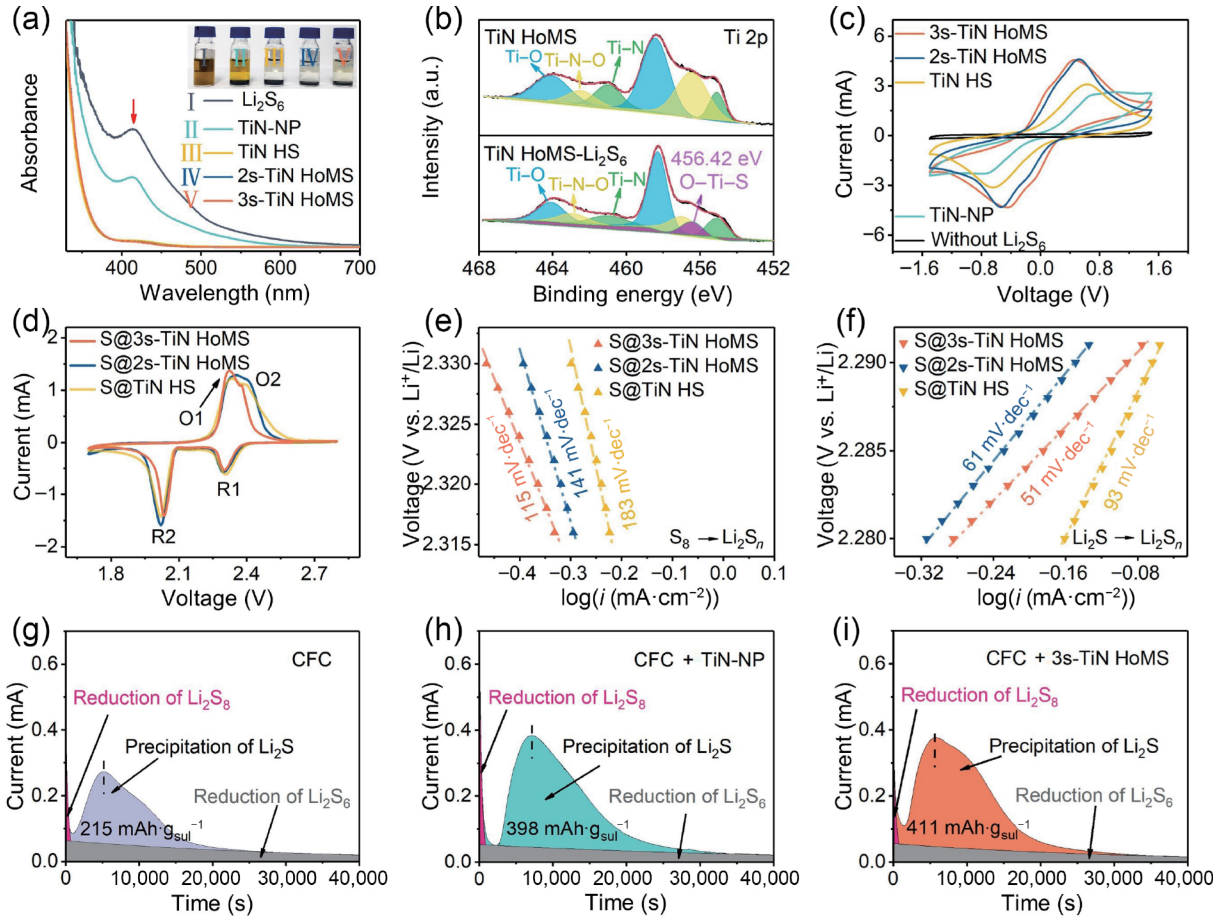

Figure 3 (a) UV–visible spectra and inserted optical images of Li_2S_6 in 1,3-dioxolane/1,2-dimethoxyethan (DOL/DME) solution and after being adsorbed by TiN-NP, TiN HS, and 2s- and 3s-TiN HoMS. (b) Ti 2p XPS spectra of TiN HoMS and TiN HoMS-Li_2S_6. (c) Polarization curves of the Li_2S_6 symmetric cell. (d) CV curves of S@TiN HoMS at 0.2 mV·s^{-1}. Tafel plots for S@TiN HoMS electrodes during (e) reduction and (f) oxidation processes. Fitting of current vs. time curves for a potentiostatic discharge at 2.02 V, (g) CFC, (h) CFC + TiN-NP, and (i) CFC + 3s-TiN HoMS.

determined by XPS measurements. Figure 3(b) illustrates an overall shift of the peaks of TiN HoMS-Li_2S_6 toward lower binding energies compared to TiN HoMS, which indicates a stronger interaction between TiN and Li_2S_6. Likewise, a similar peak shift is observed in the N 1s spectrum (Fig. S5 in the ESM). TiN HoMS-Li_2S_6 exhibits a new peak at 456.42 eV, corresponding to the formed S–Ti–O bond [60]. The above results suggest that TiN HoMS provides strong anchoring ability to LiPSs, which is conducive to confining the diffusion shuttle of LiPSs.

In addition to chemical anchoring LiPSs, TiN HoMS is able to catalyze the conversion of LiPSs and promote Li_2S nucleation and growth [61, 62]. To verify the electrocatalytic activity of TiN HoMS, a symmetric cell was assembled. As shown in Fig. 3(c), cells based on TiN HoMS electrodes show higher currents than those based on TiN-NP electrodes. Additionally, the magnitude of the current was increased with an increase in shell number in the TiN sample. The electrocatalytic activity was further verified through cyclic voltammetry (CV) and potential polarization experiments. In Fig. 3(d), the reduction peak at R1 corresponds to the reduction of S_8 molecules to soluble long-chain polysulfides (Li_2S_n, n = 4–8) during discharge process, and the reduction peak at R2 corresponds to the reduction of soluble polysulfides (Li_2S_n, n = 4–8) to electrolyte-insoluble Li_2S_2 and Li_2S [63]. Two oxidation peaks O1 and O2 correspond to the oxidation of Li_2S_2/Li_2S to S_8 during the charge process. Figures 3(e) and 3(f) show the Tafel slopes during the oxidation and reduction processes, respectively. The Tafel slopes of S@TiN HS, S@2s-TiN HoMS, and S@3s-TiN HoMS are 93, 61, and 51 mV·dec^{-1} for the Li_2S to Li_2S_n conversion and 183, 141, and 115 mV·dec^{-1} for the S_8 to Li_2S_n conversion, which further proves the electrocatalytic activity of TiN HoMS.

Normally, the reaction kinetics of the conversion from soluble polysulfide to insulating solid Li_2S is poor in the late stage of discharge process, wherein the precipitation of Li_2S greatly affects the capacity of the battery. To evaluate the effect of TiN on the precipitation of Li_2S, cells were assembled by using equal mass of TiN-NP and 3s-TiN HoMS loaded carbon fiber cloth (CFC) as cathode and lithium metal as anode. Cells were discharged to 2.06 V at a current density of 0.112 mA and then held potential at 2.05 V until the current dropped below 10^{-5} A. According to Faraday's law, the Li_2S precipitates were evaluated according to the charge [47, 64]. As shown in Figs. 3(g)–3(i), the deposition capacity of Li_2S on the surface of CFC + 3s-TiN HoMS reaches 411 mAh·g^{-1}, which is the largest among the three cells, confirming that 3s-TiN HoMS can enhance the conversion of LiPLs to Li_2S and the nucleation and growth of Li_2S. The reasons are ascribed to that the excellent electrical conductivity of TiN facilitates electron diffusion and the HoMS can shorten the transport path of ions and electrons.

The electrochemical performance is evaluated by assembling CR2032 coin cells with lithium metal used as the counter and reference electrode. Figure 4(a) shows the first-cycle charge/discharge voltage profiles of the S@3s-TiN HoMS, S@2s-TiN HoMS, S@TiN HS, S/TiN-NP, and S/C electrodes at 0.2 C. S@3s-TiN HoMS exhibits the highest specific capacity and high initial Coulombic efficiency of 98.3%. It is worth mentioning that TiN hosts have no contribution to the overall capacity by themselves (Fig. S6 in the ESM). In addition, it is worth noting that the specific capacities of the five electrodes are relatively similar in the first discharge plateau but differ dramatically in the

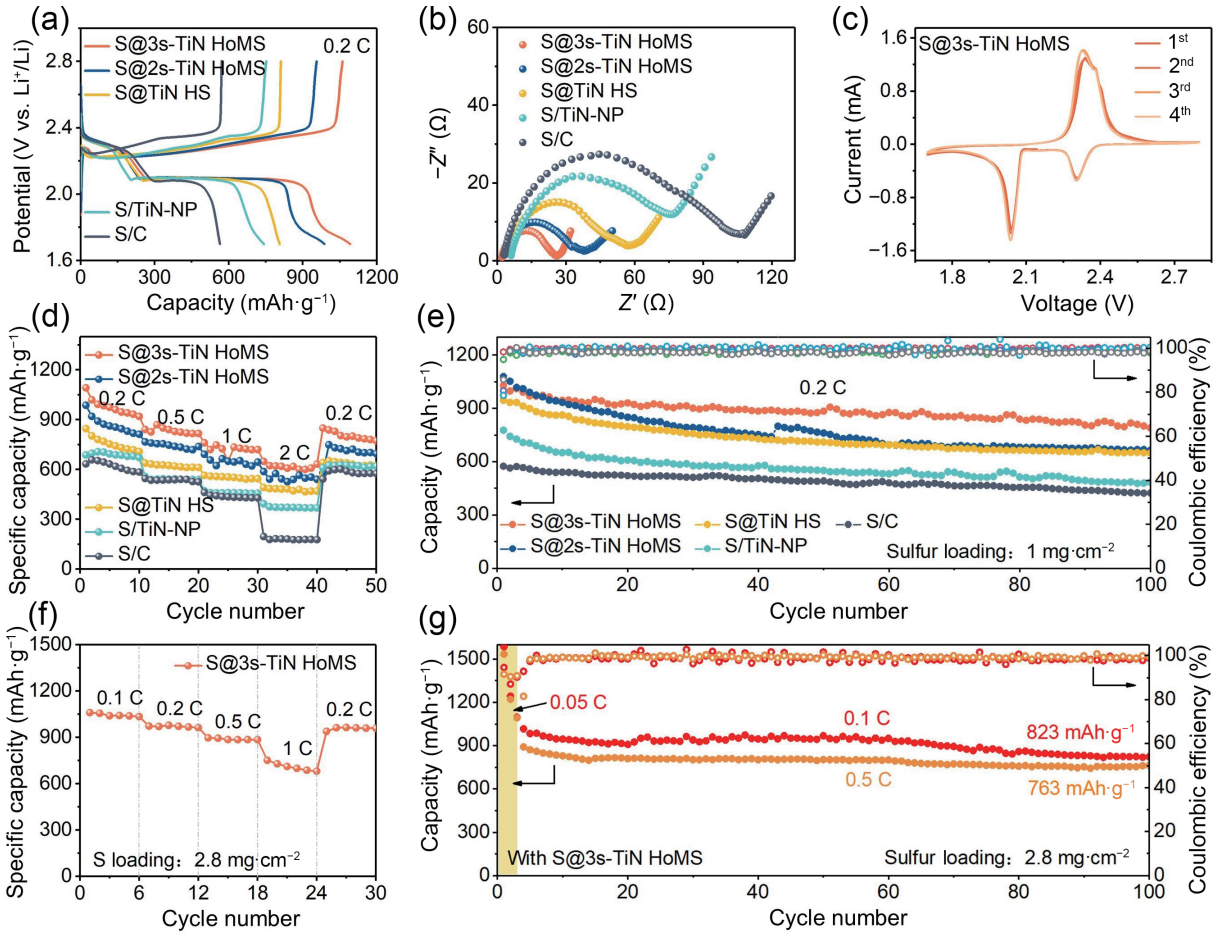

Figure 4 (a) Galvanostatic charge–discharge voltage profiles of S@TiN HoMS, S@TiN HS, S/TiN-NP, and S/C at a rate 0.2 C. (b) Nyquist plots of S@TiN HoMS, S@TiN HS, S/TiN-NP, and S/C from 0.1 to 100 MHz. (c) CV profiles of S@3s-TiN HoMS at a scan rate of 0.2 mV·s^{-1}. (d) Rate capabilities of S@TiN HoMS, S@TiN HS, S/TiN-NP, and S/C electrodes tested at 0.2, 0.5, 1, and 2 C, with a mass loading of 1.0 mg·cm^{-2}. (e) Cycling performance of S@TiN HoMS, S@TiN HS, S/TiN-NP, and S/C at 0.2 C (activated at 0.05 C was removed). (f) Rate capabilities of 2.8 mg·cm^{-2} sulfur-loaded S@3s-TiN HoMS cathode. (g) Cycle performance and Coulombic efficiency of 2.8 mg·cm^{-2} sulfur-loaded S@3s-TiN HoMS cathode at 0.1 and 0.5 C.

second discharge plateau (Fig. S8 in the ESM). The ratios of the capacity obtained in the second discharge plateau to those obtained in the first plateau for S@3s-TiN HoMS, S@2s-TiN HoMS, S@TiN HS, S/TiN-NP, and S/C are 3.1:1, 3.0:1, 2.2:, 2.0:1, and 0.9:1. It is demonstrated that 3s-TiN HoMS host enables the catalytic conversion of polysulfides more effectively.

The magnitude of the charge transfer resistance (R_{ct}) can be compared by the depressed semicircle of the Nyquist curve in the high frequency region. As shown in Fig. 4(b), the R_{ct} of S/TiN-NP is significantly lower than that of S/C due to the better conductivity of TiN (4000–55,000 S·cm^{-1}) than carbon (0.2–0.5 S·cm^{-1}) [57]. In particular, the R_{ct} of TiN HoMS decreases with the increase in the number of shells. It is due to that multiple shells are connected with each other and form a percolated conductive pathway, which is able to reduce the overall resistance of the circuit [65].

Figure 4(c) demonstrates the CV curves of the cell with the S@3s-TiN HoMS cathode in the first five cycles at 0.2 mV·s^{-1}. The CV cycle almost overlapped, demonstrating good reversibility and stability of the S@3s-TiN HoMS electrode. Moreover, the cycle performance of S@TiN HoMS composite is generally superior to the S@TiN HS, S/TiN-NP, and S/C composite (Fig. 4(e)). Specifically, S@3s-TiN HoMS achieves the highest capacity of 790 mAh·g^{-1} after 100 cycles at 0.2 C, followed by S@2s-TiN HoMS (663 mAh·g^{-1}), S@TiN HS (648 mAh·g^{-1}), S/TiN-NP (648 mAh·g^{-1}), and S/C (424 mAh·g^{-1}). Figure 4(d) shows the rate capability at 0.2, 0.5, 1, 2, and 0.2 C rate, respectively. Obviously, the S@TiN HoMS exhibited a better rate capability compared to S@TiN HS, S/TiN-NP, and S/C, delivering a discharge capacity of 1019, 869, 747, and 618 mAh·g^{-1} at 0.2, 0.5, 1, and 2 C rate, respectively. Moreover, the discharge capacity can almost be recovered to the similar value when the current density decreases back to 0.2 C, indicating that S@3s-TiN HoMS has excellent multiplicative performance. This is mainly due to the shortened ion and electron transport path and the effective confinement of LiPSs by TiN HoMSs.

Considering the requirements of practical application, electrochemical performance with a high sulfur loading is explored. When the sulfur loading was increased to 2.8 mg·cm^{-2}, the cathodes of S@3s-TiN HoMS still performed a good rate capability, showing discharge capacities of 1060, 970, 896, and 751 mAh·g^{-1} at 0.1, 0.2, 0.5, and 1 C rate, respectively (Fig. 4(f)). When the rate was switched back from 1 to 0.2 C, the discharge capacity recovered to 964 mAh·g^{-1}. In addition, the cycle life of the S@3s-TiN HoMS electrode with areal sulfur loading of 2.8 mg·cm^{-2} was tested at 0.2 and 0.5 C for 100 cycles (Fig. 4(g)). Upon the initial activation cycle at 0.05 C, the discharge capacities of 1585 and 1534 mAh·g^{-1} are delivered, corresponding to an areal capacity of 4.4 and 4.3 mAh·cm^{-2}, respectively. The S@3s-TiN HoMS electrode delivers capacities of 1016 mAh·g^{-1} (2.8 mAh·cm^{-2}) at 0.1 C and 891 mAh·g^{-1} (2.5 mAh·cm^{-2}) at 0.5 C, respectively. The capacities are stabilized at above 823 mAh·g^{-1} (2.3 mAh·cm^{-2}) and 763 mAh·g^{-1} (2.1 mAh·cm^{-2}) over 100 cycles, respectively, which is attributed to the good conductivity of TiN and its effective catalytic effect promoting the conversion of LiPSs.

To further understand the reaction mechanism, *in situ* Raman

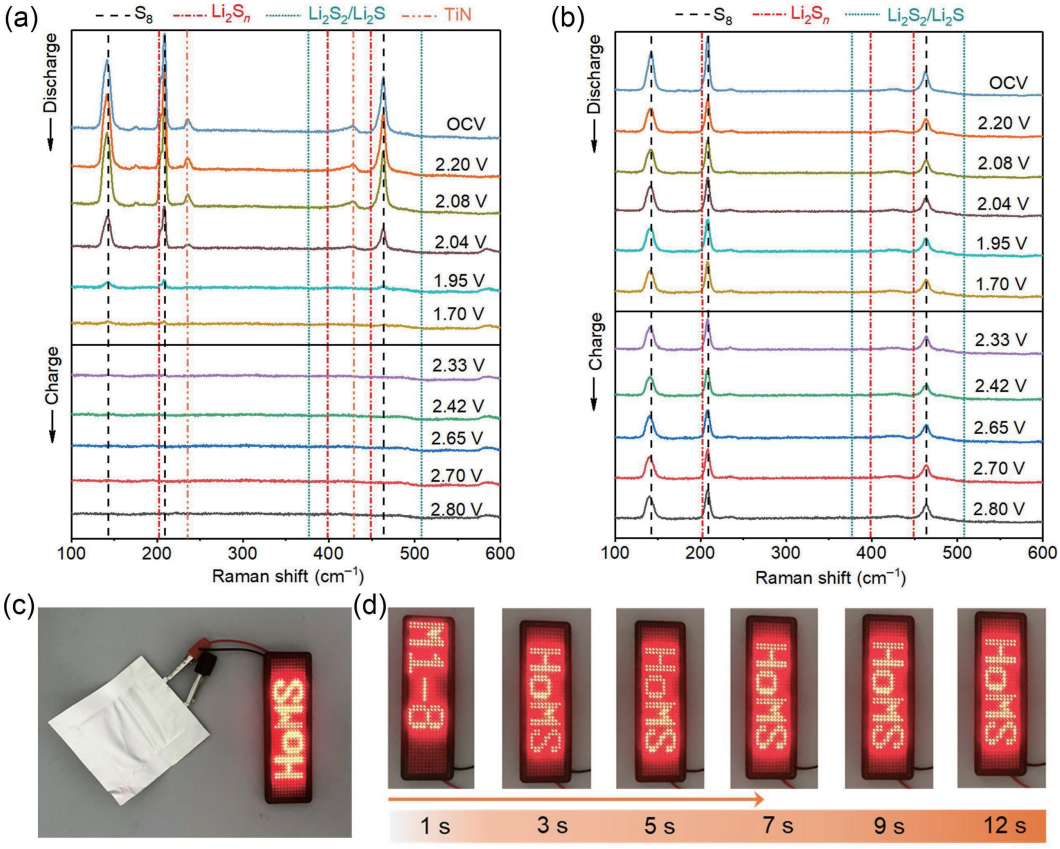

Figure 5 *In situ* Raman spectra of Li-S batteries based on (a) S@3s-TiN HoMS and (b) S/C cathodes during the discharge–charge processes. Pouch cells were assembled by pairing S@3s-TiN HoMS cathode with Li foil anode, (c) LED display light lighting test and (d) long-time bright screen test of LED display.

spectroscopy was carried out to monitor the real-time evolution of sulfur species. Figures 5(a) and 5(b) depict the *in situ* Raman spectra obtained for S@3s-TiN HoMS and S/C cathode surface, respectively, during the discharge–charge process. Characteristic peaks around 145, 211, and 463 cm^{-1} corresponding to S_8^{2-} can be observed at the beginning of the discharge process for these two cathodes [66, 67]. As for the S@3s-TiN HoMS cathode, characteristic peaks around 232 and 427 cm^{-1} corresponding to TiN can also be observed. With the continuous discharge, the peaks of S_8^{2-} became weaker and totally disappeared at the end of discharge process, indicating that S_8^{2-} has been totally converted and no S_8^{2-} species has been transported to the anode side. In addition, the signal of S_8^{2-} gradually re-appeared during the charge process, indicating the reversible and fast redox reaction. In contrast, as for the S/C cathode, the peaks of S_8^{2-} were slightly weakened and could be observed during the whole discharge process, indicating that the reduction reaction of S_8^{2-} was incomplete, which may be ascribed to the severe shuttle effect happened in the S/C cathode. To further investigate the practicability of 3s-TiN HoMS host, a pouch cell based on S@3s-TiN HoMS cathode and lithium foil anode was constructed. As shown in Figs. 5(c) and 5(d), this pouch cell could easily and continually power the light-emitting diode (LED) screen with a "HOMS" pattern.

3 Conclusions

In summary, TiN HoMS was synthesized and employed as a catalytic host for S cathode. TiN not only improves the conductivity of sulfur cathode but also promotes the redox reaction kinetics, and its strong adsorption ability of lithium polysulfide effectively inhibits the LiPSs shuttle effect. Meanwhile, HoMS not only effectively buffers the volume expansion of S but also shortens the ion and electron transport pathways, as well as inhibits shuttle effect by providing abundant adsorption sites and multiple physical barriers. As a result, 3s-TiN HoMS simultaneously exhibits a high specific capacity, good cycling stability, and superior rate capability, reaching an initial specific capacity of 1016 $mAh \cdot g^{-1}$ and maintained at 823 $mAh \cdot g^{-1}$ after 100 cycles with a high sulfur loading of 2.8 $mg \cdot cm^{-2}$, and showing a four times high specific capacity than the one without TiN host at 2 C. This work provides novel insight into the design of multi-functional hosts for Li-S batteries with better multiplicative performance, high capacity, and long cycle stability.

Acknowledgements

This study received support from the National Natural Science Foundation of China (Nos. 21820102002, 52301296, 51932001, 52372170, and 52261160573), the National Key R&D Program (Nos. 2018YFA0703503, 2021YFC2902503, and 2022YFA1504101), the Cooperation Fund of the Institute of Clean Energy Innovation, Chinese Academy of Sciences (No. DNL202020), the Zhongke-Yuneng Joint R&D Center Program (No. ZKYN2022008), and Institute of Process Engineering (IPE) Project for Frontier Basic Research (No. QYJC-2022-008).

Electronic Supplementary Material: Supplementary material (the detailed process of material synthesis, battery assembly, material characterization methods (SEM measurements, TEM imaging, BET measurements, X-ray powder diffraction, X-ray photoelectron spectra, etc.), and partial battery performance characterization data) is available in the online version of this article at https://doi.org/10.1007/s12274-023-6144-6.

References

[1] Evers, S.; Nazar, L. F. New approaches for high energy density

lithium-sulfur battery cathodes. *Acc. Chem. Res.* **2013**, *46*, 1135–1143.

[2] Li, H.; Song, J. P.; Wu, F. L.; Wang, R.; Liu, D.; Tang, H. L. Metal-nitrogen-doped hybrid ionic/electronic conduction triple-phase interfaces for high-performance all-solid-state lithium-sulfur batteries. *Nano Res.* **2023**, *16*, 10956–10965.

[3] Ji, X. L.; Lee, K. T.; Nazar, L. F. A highly ordered nanostructured carbon-sulphur cathode for lithium-sulphur batteries. *Nat. Mater.* **2009**, *8*, 500–506.

[4] Yang, M.; Bi, R. Y.; Wang, J. Y.; Yu, R. B.; Wang, D. Decoding lithium batteries through advanced *in situ* characterization techniques. *Int. J. Miner. Metall. Mater.* **2022**, *29*, 965–989.

[5] Ye, H. L.; Li, Y. G. Towards practical lean-electrolyte Li–S batteries: Highly solvating electrolytes or sparingly solvating electrolytes? *Nano Res. Energy* **2022**, *1*, e9120012.

[6] Liu, Y. S.; Zhao, X. H.; Li, S. S.; Zhang, Q.; Wang, K. X.; Chen, J. S. Towards high-performance lithium-sulfur batteries: The modification of polypropylene separator by 3D porous carbon structure embedded with Fe_3C/Fe nanoparticles. *Chem. Res. Chin. Univ.* **2022**, *38*, 147–154.

[7] Wang, F.; Zuo, Z. C.; Li, L.; He, F.; Li, Y. L. Graphdiyne nanostructure for high-performance lithium-sulfur batteries. *Nano Energy* **2019**, *68*, 104307.

[8] Li, B. Q.; Peng, H. J.; Chen, X.; Zhang, S. Y.; Xie, J.; Zhao, C. X.; Zhang, Q. Polysulfide electrocatalysis on framework porphyrin in high-capacity and high-stable lithium-sulfur batteries. *CCS Chem.* **2019**, *1*, 128–137.

[9] Lu, R. C.; Cheng, M.; Mao, L. J.; Zhang, M.; Yuan, H. X.; Amin, K.; Yang, C.; Cheng, Y. L.; Meng, Y. N.; Wei, Z. X. Nitrogen-doped nanoarray-modified 3D hierarchical graphene as a cofunction host for high-performance flexible Li-S battery. *EcoMat* **2020**, *2*, e12010.

[10] Du, L. Y.; Wang, H. M.; Yang, M.; Liu, L. L.; Niu, Z. Q. Free-standing nanostructured architecture as a promising platform for high-performance lithium-sulfur batteries. *Small Struct.* **2020**, *1*, 2000047.

[11] Razaq, R.; Zhang, N. N.; Xin, Y.; Li, Q.; Wang, J.; Zhang, Z. L. Electrocatalytic conversion of lithium polysulfides by highly dispersed ultrafine Mo_2C nanoparticles on hollow N-doped carbon flowers for Li-S batteries. *EcoMat* **2020**, *2*, e12020.

[12] Pan, H.; Cheng, Z. B.; Fransaer, J.; Luo, J. S.; Wübbenhorst, M. Cobalt-embedded 3D conductive honeycomb architecture to enable high-sulphur-loading Li-S batteries under lean electrolyte conditions. *Nano Res.* **2022**, *15*, 8091–8100.

[13] Liu, H. T.; Liu, F.; Qu, Z. H.; Chen, J. L.; Liu, H.; Tan, Y. Q.; Guo, J. B.; Yan, Y.; Zhao, S.; Zhao, X. S. et al. High sulfur loading and shuttle inhibition of advanced sulfur cathode enabled by graphene network skin and N, P, F-doped mesoporous carbon interfaces for ultra-stable lithium sulfur battery. *Nano Res. Energy* **2023**, *2*, e9120049.

[14] Li, Z.; Hou, L. P.; Zhang, X. Q.; Li, B. Q.; Huang, J. Q.; Chen, C. M.; Liu, Q. B.; Xiang, R.; Zhang, Q. A Nafion protective layer for stabilizing lithium metal anodes in working lithium-sulfur batteries. *Battery Energy.* **2022**, *1*, 20220006.

[15] Wang, C. D.; Ma, Y.; Du, X. F.; Zhang, H. R.; Xu, G. J.; Cui, G. L. A polysulfide radical anions scavenging binder achieves long-life lithium-sulfur batteries. *Battery Energy.* **2022**, *1*, 20220010.

[16] Wei Seh, Z.; Li, W. Y.; Cha, J. J.; Zheng, G. Y.; Yang, Y.; McDowell, M. T.; Hsu, P. C.; Cui, Y. Sulphur-TiO_2 yolk–shell nanoarchitecture with internal void space for long-cycle lithium-sulphur batteries. *Nat. Commun.* **2013**, *4*, 1331.

[17] Li, Z.; Zhang, J. T.; Guan, B. Y.; Wang, D.; Liu, L. M.; Lou, X. W. A sulfur host based on titanium monoxide@carbon hollow spheres for advanced lithium-sulfur batteries. *Nat Commun.* **2016**, *7*, 13065.

[18] Zhang, C.; Liu, D. H.; Geng, C. N.; Hua, W. X.; Tang, Q. J.; Ling, G. W.; Yang, Q. H. Solution-based preparation of high sulfur content sulfur/graphene cathode material for Li-S battery. *Chem. Res. Chin. Univ.* **2021**, *37*, 323–327.

[19] Huang, X.; Qiu, T. F.; Zhang, X. H.; Wang, L.; Luo, B.; Wang, L. Z. Recent advances of hollow-structured sulfur cathodes for lithium-sulfur batteries. *Mater. Chem. Front.* **2020**, *4*, 2517–2547.

[20] Yuan, K.; Yuan, L. X.; Chen, J.; Xiang, J. W.; Liao, Y. Q.; Li, Z.; Huang, Y. H. Methods and cost estimation for the synthesis of nanosized lithium sulfide. *Small Struct.* **2021**, *2*, 2000059.

[21] Wang, L.; Li, G. R.; Liu, S.; Gao, X. P. Hollow molybdate microspheres as catalytic hosts for enhancing the electrochemical performance of sulfur cathode under high sulfur loading and lean electrolyte. *Adv. Funct. Mater.* **2021**, *31*, 2010693.

[22] Chen, W. J.; Xia, H. C.; Guo, K.; Jin, W. Z.; Du, Y.; Yan, W. F.; Qu, G.; Zhang, J. N. Atomically dispersed Fe-N_4 sites and Fe_3C particles catalyzing polysulfides conversion in Li-S batteries. *Chem. Res. Chin. Univ.* **2022**, *38*, 1232–1238.

[23] Qian, J.; Xing, Y.; Yang, Y.; Li, Y.; Yu, K. X.; Li, W. L.; Zhao, T.; Ye, Y. S.; Li, L.; Wu, F. et al. Enhanced electrochemical kinetics with highly dispersed conductive and electrocatalytic mediators for lithium-sulfur batteries. *Adv. Mater.* **2021**, *33*, e2100810.

[24] Zhang, J. T.; Hu, H.; Li, Z.; Lou, X. W. Double-shelled nanocages with cobalt hydroxide inner shell and layered double hydroxides outer shell as high-efficiency polysulfide mediator for lithium-sulfur batteries. *Angew. Chem., Int. Ed.* **2016**, *55*, 3982–3986.

[25] Salhabi, E. H. M.; Zhao, J. L.; Wang, J. Y.; Yang, M.; Wang, B.; Wang, D. Hollow multi-shelled structural TiO_{2-x} with multiple spatial confinement for long-life lithium-sulfur batteries. *Angew. Chem., Int. Ed.* **2019**, *58*, 9078–9082.

[26] Wei, Y. Z.; You, F. F.; Zhao, D. C.; Wan, J. W.; Gu, L.; Wang, D. Heterogeneous hollow multi-shelled structures with amorphous-crystalline outer-shells for sequential photoreduction of CO_2. *Angew. Chem., Int. Ed.* **2022**, *61*, e202212049.

[27] Zhao, D. C.; Wei, Y. Z.; Jin, Q.; Yang, N. L.; Yang, Y.; Wang, D. PEG-functionalized hollow multishelled structures with on-off switch and rate-regulation for controllable antimicrobial release. *Angew. Chem., Int. Ed.* **2022**, *61*, e202206807.

[28] Wei, Y. Z.; Wan, J. W.; Yang, N. L.; Yang, Y.; Ma, Y. W.; Wang, S. C.; Wang, J. Y.; Yu, R. B.; Gu, L.; Wang, L. H. et al. Efficient sequential harvesting of solar light by heterogeneous hollow shells with hierarchical pores. *Natl. Sci. Rev.* **2020**, *7*, 1638–1646.

[29] Chen, X. B.; Yang, N. L.; Wang, Y. L.; He, H. Y.; Wang, J. Y.; Wan, J. W.; Jiang, H. Y.; Xu, B.; Wang, L. M.; Yu, R. B. et al. Highly efficient photothermal conversion and water transport during solar evaporation enabled by amorphous hollow multishelled nanocomposites. *Adv. Mater.* **2022**, *34*, 2107400.

[30] Zhao, D. C.; Yang, N. L.; Wei, Y.; Jin, Q.; Wang, Y. L.; He, H. Y.; Yang, Y.; Han, B.; Zhang, S. J.; Wang, D. Sequential drug release via chemical diffusion and physical barriers enabled by hollow multishelled structures. *Nat. Commun.* **2020**, *11*, 4450.

[31] Wang, L.; Wan, J. W.; Wang, J. Y.; Wang, D. Small structures bring big things: Performance control of hollow multishelled structures. *Small Struct.* **2021**, *2*, 2000041.

[32] Zhang, Y. T.; Ran, L.; Li, Z. W.; Zhai, P. L.; Zhang, B.; Fan, Z. Z.; Wang, C.; Zhang, X. M.; Hou, J. G.; Sun, L. C. Simultaneously efficient solar light harvesting and charge transfer of hollow octahedral Cu_2S/CdS p–n heterostructures for remarkable photocatalytic hydrogen generation. *Trans. Tianjin Univ.* **2021**, *27*, 348–357.

[33] Wang, J. Y.; Yang, M.; Wang, D. Progress and perspectives of hollow multishelled structures. *Chin. J. Chem.* **2022**, *40*, 1190–1203.

[34] Wang, J. Y.; Tang, H. J.; Zhang, L. J.; Ren, H.; Yu, R. B.; Jin, Q.; Qi, J.; Mao, D.; Yang, M.; Wang, Y. et al. Multi-shelled metal oxides prepared via an anion-adsorption mechanism for lithium-ion batteries. *Nat. Energy* **2016**, *1*, 16050.

[35] Wang, J. Y.; Wan, J. W.; Yang, N. L.; Li, Q.; Wang, D. Hollow multishell structures exercise temporal–spatial ordering and dynamic smart behaviour. *Nat. Rev. Chem.* **2020**, *4*, 159–168.

[36] Luo, D.; Li, G. R.; Deng, Y. P.; Zhang, Z.; Li, J. D.; Liang, R. L.; Li, M.; Jiang, Y.; Zhang, W. W.; Liu, Y. S. et al. Synergistic engineering of defects and architecture in binary metal chalcogenide toward fast and reliable lithium-sulfur batteries. *Adv. Energy Mater.* **2019**, *9*, 1900228.

[37] Mao, D.; Wan, J. W.; Wang, J. Y.; Wang, D. Sequential templating approach: A groundbreaking strategy to create hollow multishelled structures. *Adv. Mater.* **2019**, *31*, 1802874.

[38] Zhao, J. L.; Wang, J. Y.; Bi, R. Y.; Yang, M.; Wan, J. W.; Jiang, H.

Y.; Gu, L.; Wang, D. General synthesis of multiple-cores@multiple-shells hollow composites and their application to lithium-ion batteries. *Angew. Chem., Int. Ed.* **2021**, *60*, 25719–25722.

[39] Wang, J. Y.; Wang, Z. M.; Mao, D.; Wang, D. The development of hollow multishelled structure: From the innovation of synthetic method to the discovery of new characteristics. *Sci. China Chem.* **2022**, *65*, 7–19.

[40] Li, B.; Bi, R. Y.; Yang, M.; Gao, W.; Wang, J. Y. Coating conductive polypyrrole layers on multiple shells of hierarchical SnO_2 spheres and their enhanced cycling stability as lithium-ion battery anode. *Appl. Surf. Sci.* **2022**, *586*, 152836.

[41] Li, B.; Wang, J. Y.; Bi, R. Y.; Yang, N. L.; Wan, J. W.; Jiang, H. Y.; Gu, L.; Du, J.; Cao, A. M.; Gao, W. et al. Accurately localizing multiple nanoparticles in a multishelled matrix through shell-to-core evolution for maximizing energy-storage capability. *Adv. Mater.* **2022**, *34*, 2200206.

[42] Zhou, T. H.; Lv, W.; Li, J.; Zhou, G. M.; Zhao, Y.; Fan, S. X.; Liu, B. L.; Li, B. H.; Kang, F. Y.; Yang, Q. H. Twinborn TiO_2–TiN heterostructures enabling smooth trapping–diffusion–conversion of polysulfides towards ultralong life lithium-sulfur batteries. *Energy Environ. Sci.* **2017**, *10*, 1694–1703.

[43] Cui, Z. M.; Zu, C. X.; Zhou, W. D.; Manthiram, A.; Goodenough, J. B. Mesoporous titanium nitride-enabled highly stable lithium-sulfur batteries. *Adv. Mater.* **2016**, *28*, 6926–6931.

[44] Qi, B.; Zhao, X. S.; Wang, S. G.; Chen, K.; Wei, Y. J.; Chen, G.; Gao, Y.; Zhang, D.; Sun, Z. H.; Li, F. Mesoporous TiN microspheres as an efficient polysulfide barrier for lithium-sulfur batteries. *J. Mater. Chem. A* **2018**, *6*, 14359–14366.

[45] Deng, D. R.; An, T. H.; Li, Y. J.; Wu, Q. H.; Zheng, M. S.; Dong, Q. F. Hollow porous titanium nitride tubes as a cathode electrode for extremely stable Li-S batteries. *J. Mater. Chem. A* **2016**, *4*, 16184–16190.

[46] Yao, Y.; Wang, H. Y.; Yang, H.; Zeng, S. F.; Xu, R.; Liu, F. F.; Shi, P. C.; Feng, Y. Z.; Wang, K.; Yang, W. J. et al. A dual-functional conductive framework embedded with TiN–VN heterostructures for highly efficient polysulfide and lithium regulation toward stable Li-S full batteries. *Adv. Mater.* **2020**, *32*, 1905658.

[47] Wang, Y. K.; Zhang, R. F.; Pang, Y. C.; Chen, X.; Lang, J. X.; Xu, J. J.; Xiao, C. H.; Li, H. L.; Xi, K.; Ding, S. J. Carbon@titanium nitride dual shell nanospheres as multi-functional hosts for lithium sulfur batteries. *Energy Storage Mater.* **2019**, *16*, 228–235.

[48] Mosavati, N.; Chitturi, V. R.; Salley, S. O.; Ng, K. Y. S. Nanostructured titanium nitride as a novel cathode for high performance lithium/dissolved polysulfide batteries. *J. Power Sources* **2016**, *321*, 87–93.

[49] Li, Z.; Zhang, J. T.; Guan, B. Y.; Lou, X. W. Mesoporous carbon@titanium nitride hollow spheres as an efficient SeS_2 host for advanced Li-SeS_2 batteries. *Angew. Chem., Int. Ed.* **2017**, *56*, 16003–16007.

[50] Yu, Y.; Yan, M.; Dong, W. D.; Wu, L.; Tian, Y. W.; Deng, Z.; Chen, L. H.; Hasan, T.; Li, Y.; Su, B. L. Optimizing inner voids in yolk–shell TiO_2 nanostructure for high-performance and ultralong-life lithium-sulfur batteries. *Chem. Eng. J.* **2021**, *417*, 129241.

[51] Zhang, C. F.; Wu, H. B.; Yuan, C. Z.; Guo, Z. P.; Lou, X. W. Confining sulfur in double-shelled hollow carbon spheres for lithium-sulfur batteries. *Angew. Chem., Int. Ed.* **2012**, *51*, 9592–9595.

[52] Tan, X. N.; Wang, X. G.; Wang, X. Q.; Wang, Y. F.; Li, C.; Xia, D. G. $NiCo_2S_4$ yolk–shell hollow spheres with physical and chemical interaction toward polysulfides for advanced lithium-sulfur batteries. *Ionics* **2019**, *25*, 4047–4056.

[53] Zhu, Y. J.; Wang, J. Y.; Xie, C.; Yang, M.; Zheng, Z. J.; Yu, R. B. Hollow multishelled structural NiO as a "shelter" for high-performance Li-S batteries. *Mater. Chem. Front.* **2020**, *4*, 2971–2975.

[54] Wei, Y. Z.; Cheng, Y. P.; Zhao, D. C.; Feng, Y.; Wei, P.; Wang, J. Y.; Ge, W.; Wang, D. A universal formation mechanism of hollow multi-shelled structures dominated by concentration waves. *Angew. Chem., Int. Ed.* **2023**, *62*, e202302621.

[55] Qi, J.; Lai, X. Y.; Wang, J. Y.; Tang, H. J.; Ren, H.; Yang, Y.; Jin, Q.; Zhang, L. J.; Yu, R. B.; Ma, G. H. et al. Multi-shelled hollow micro-/nanostructures. *Chem. Soc. Rev.* **2015**, *44*, 6749–6773.

[56] Li, Z. M.; Lai, X. Y.; Wang, H.; Mao, D.; Xing, C. J.; Wang, D. General synthesis of homogeneous hollow core–shell ferrite microspheres. *J. Phys. Chem. C* **2009**, *113*, 2792–2797.

[57] Lai, X. Y.; Li, J.; Korgel, B. A.; Dong, Z. H.; Li, Z. M.; Su, F. B.; Du, J.; Wang, D. General synthesis and gas-sensing properties of multiple-shell metal oxide hollow microspheres. *Angew. Chem., Int. Ed.* **2011**, *50*, 2738–2741.

[58] Ren, H.; Yu, R. B.; Wang, J. Y.; Jin, Q.; Yang, M.; Mao, D.; Kisailus, D.; Zhao, H. J.; Wang, D. Multishelled TiO_2 hollow microspheres as anodes with superior reversible capacity for lithium ion batteries. *Nano Lett.* **2014**, *14*, 6679–6684.

[59] Sun, X. M.; Li, Y. D. Colloidal carbon spheres and their core/shell structures with noble-metal nanoparticles. *Angew. Chem., Int. Ed.* **2004**, *43*, 597–601.

[60] Liao, Y. Q.; Xiang, J. W.; Yuan, L. X.; Hao, Z. X.; Gu, J. F.; Chen, X.; Yuan, K.; Kalambate, P. K.; Huang, Y. H. Biomimetic root-like TiN/C@S nanofiber as a freestanding cathode with high sulfur loading for lithium-sulfur batteries. *ACS Appl. Mater. Interfaces* **2018**, *10*, 37955–37962.

[61] Huang, S. Z.; Lim, Y. V.; Zhang, X. M.; Wang, Y.; Zheng, Y.; Kong, D. Z.; Ding, M.; Yang, S. A.; Yang, H. Y. Regulating the polysulfide redox conversion by iron phosphide nanocrystals for high-rate and ultrastable lithium-sulfur battery. *Nano Energy* **2018**, *51*, 340–348.

[62] Fan, F. Y.; Carter, W. C.; Chiang, Y. M. Mechanism and kinetics of Li_2S precipitation in lithium-sulfur batteries. *Adv. Mater.* **2015**, *27*, 5203–5209.

[63] Wild, M.; O'Neill, L.; Zhang, T.; Purkayastha, R.; Minton, G.; Marinescu, M.; Offer, G. J. Lithium sulfur batteries, a mechanistic review. *Energy Environ. Sci.* **2015**, *8*, 3477–3494.

[64] Li, Z. J.; Zhou, Y. C.; Wang, Y.; Lu, Y. C. Solvent-mediated Li_2S electrodeposition: A critical manipulator in lithium-sulfur batteries. *Adv. Energy Mater.* **2019**, *9*, 1802207.

[65] Bi, R. Y.; Xu, N.; Ren, H.; Yang, N. L.; Sun, Y. G.; Cao, A. M.; Yu, R. B.; Wang, D. A hollow multi-shelled structure for charge transport and active sites in lithium-ion capacitors. *Angew. Chem., Int. Ed.* **2020**, *59*, 4865–4868.

[66] Mahankali, K.; Thangavel, N. K.; Gopchenko, D.; Arava, L. M. R. Atomically engineered transition metal dichalcogenides for liquid polysulfide adsorption and their effective conversion in Li-S batteries. *ACS Appl. Mater. Interfaces* **2020**, *12*, 27112–27121.

[67] Zhu, W.; Paolella, A.; Kim, C. S.; Liu, D.; Feng, Z.; Gagnon, C.; Trottier, J.; Vijh, A.; Guerfi, A.; Mauger, A. et al. Investigation of the reaction mechanism of lithium sulfur batteries in different electrolyte systems by *in situ* Raman spectroscopy and *in situ* X-ray diffraction. *Sustainable Energy Fuels* **2017**, *1*, 737–747.